Photovoltage detection of spin excitation of ferromagnetic stripe and disk at low temperature

Najla K. Almulhem[1,2*], Maksym E. Stebliy[3], Jean-Claude Portal[4], Alexander *S*. Samardak[3,] Harvey E. Beere[5], and David A. Ritchie[5] , Alain Nogaret[1]

[1]*Department of Physics, University of Bath, Bath, BA2 7AY, UK*

[2]*Physics Department, Faculty of Science, King Faisal University, Al-Hassa, P.O.Box 400, Hofouf 31982, Saudi Arabia*

[3]*School of Natural Sciences, Far Eastern Federal University, Vladivostok 690950, Russia.*

[4]*High Magnetic Field Laboratory, CNRS 38042 Grenoble, France*

[5]*Cavendish Laboratory, Cambridge CB3 0HE, UK*

[*]E-mail: nalmulhem@kfu.edu.sa

[*]E-mail: n.k.a.almulhem@bath.ac.uk

Photovoltage spectroscopy is a beneficial technique to investigate the dynamic properties of the spin excitations of ferromagnetic elements fabricated at the surface of a $GaAs/Al_{0.33}Ga_{0.67}As$ heterojunction. This method is of particular interest for probing localized spin wave modes. The high sensitivity of the photovoltage technique arises from the high electron mobility of 2D electrons $\mu = 1.5 \times 10^6\ cm^2.V^{-1}.S^{-1}$, which enables efficient rectification of magnetic moment oscillations through the Hall effect. We report on the discrete structure of spin wave eigenmodes as a function of magnetic field orientation, the shape of Co ferromagnets, and the geometry of nanomagnets. We indicated bonding-antibonding spin waves when B_a is parallel to the short side of the stripe at different microwave frequencies at 4K. We also observed Damon-Eshbach modes when B_a is parallel to the stripe. Micromagnetic simulations confirm the experimental results. We observe the discrete structure of the photovoltage for individual dots. We also investigate the effect of the magnetocrystalline anisotropy field of Co on ferromagnetic resonance. Our results demonstrate that photovoltage measurements in hybrid semiconductor-ferromagnetic structures provide a sensitive and extended tool for probing the spin waves of small magnets with a size of 80 nm.

1. Introduction

The technological development in microelectronics has motivated new studies in nanosized ferromagnets. The magnetic excitation in nanostructured magnets can be measured by several techniques such as magnetic resonance force microscopy,[1)] time-resolved magneto-optical Kerr effect,[2)] scanning x-ray transmission microscopy,[3)] Brillouin Light Scattering,[4, 5)] and ferromagnetic resonance spectroscopy.[6)] Spin rectification is an attractive technique to investigate dynamic magnetic properties, in particular, the spin excitations of ferromagnetic elements.[7-9)] This method is one of particular interest method for probing localized spin wave modes. The localization of spin waves states has been utilized in many applications such as spintronic devices to be used in phase-resolved microwave sensing techniques and magnetic memories, which are relevant to high-density information storage.[10-12)] Originally, spin oscillations are known to induce dc voltages through rectification effects, which depend on the nonlinear coupling between spin and charge, such as the Hall effect. [13-15)] We present our devices, which contains Co nanomagnets situated at the center of a Hall bar system. These nanomagnets were fabricated at the surface of $GaAs/Al_{0.33}Ga_{0.67}As$ heterojunction forming a two-dimensional electron gas (2DEG) to provide efficient rectification of ac oscillations of the magnetization.[16-19)] Central to these studies is the formation of spin waves on the edges of small magnets. At different microwave frequencies, the magnetostatic boundary conditions constrain spin wave modes to the surface of magnetic materials. We report on the discrete structure of spin wave resonances (SWR) as a function of the magnetic field orientation, and the shape of the Cobalt magnet (stripe or dot). The results show: (i) Strong bulk-edge mode coupling was observed as bonding-antibonding spin waves when B_a is parallel to the short side of the rectangular magnetic stripe at different frequencies. (ii) Damon-Eshbach modes were observed when B_a is parallel to the long side of the stripe.[16, 20-22)] (iii) A discrete structure of spin wave resonance SWR for magnetic dots of nanometers in size that were magnetized parallel to the 2DEG by the static magnetic field. (iv) The experimental and theoretical results simulating the imaginary susceptibility of micromagnets using Object-Oriented Micromagnetic Framework (OOMMF) program.[23)] (v) Ferromagnetic resonances have shifted according to the effect of magnetocrystalline anisotropy.[24-26)] However, the nature of photovoltage measurements in hybrid semiconductor-ferromagnetic structures provides a sensitive and extended tool for probing the localization of spin waves of small magnets of scale $\leq$100 nm.

2. Materials and Method

2.1 Setup and Devices

We designed a microwave bench at the preliminary study of photovoltage detection at the low magnetic field (<1T) and low frequency. The temperature range for this experiment was 77 K – 300 K which allowed us to demonstrate the principle of detecting spin resonance via the photovoltage. The sample was placed in the middle of two NdFeB permanent magnets. Above the sample was a microstrip antenna holder. The distance between the magnets was varied symmetrically by a Whitworth screw that displaces magnets horizontally, as shown in Fig. 1. This varying distance led to the magnetic field to vary at the site of the sample from 0.083 to 0.606 T. All measurements were performed at spin using a cold finger. The base of the cold finger was a polytetrafluoroethylene (PTFE) pot with a copper base fastened to the bottom of the pot. The pot is filled with liquid nitrogen, which chills the copper apparatus and thus the sample down to a temperature near 77 K. The microwave bench was controlled by a LabVIEW program to monitor the distance between the NdFeB magnets, enabling the study of photovoltage spectroscopy of the magnetic excitations. Each device consists of a Hall bar that has a rectangular active region with a series of arms on either side. The region was 8 μm wide and 32 μm long and was prepared by optical lithography whereas the arms are voltage probes and both ends of the Hall bar act as current probes. The voltage probes were separated by 2 - 16 μm gaps.[27] At the end of the probes is an Ohmic contact, and the Hall bars are useful tools for studying quantum transport, as shown in Fig. 2(a). We detected the collective and localized spin wave modes by measuring the photovoltage between two probes that are separated by 8 μm.

This work studies the spin dynamics in Co nanomagnets where an inhomogeneous magnetic field near the poles of the magnet confine localized spin wave modes.[4, 7-9] Figure 2(b) shows a high-resolution SEM micrograph of a Co stripe that is 80 nm wide and 30 nm thick in the active region of a Hall bar. Figure 2(c) illustrates a high-resolution SEM micrograph of a single dot that had an 80.99 nm diameter, 40 nm thickness, and was magnetized parallel to the 2DEG by B_a.

2.2 Photovoltage Measurement

The hybrid ferromagnetic-semiconductor structures use two-dimensional electron gases in $GaAs/Al_{0.33}Ga_{0.67}As$ heterojunctions. 2D electrons are located at the interface between the two layers. The 2DEG was formed 30 nm below the surface. At T = 4 K, the 2DEG had a high charge carrier mobility and low electron density of $\mu = 1.5 \times 10^6\ cm^2.V^{-1}.S^{-1}$ and $n_s = 1.6 \times$

$10^{11}\ cm^{-2}$, respectively. The high sensitivity of photovoltage measurement provides higher rectification effects than in metal structures.[28-31] In the low-magnetic-field experiment, the continuous microwave frequencies $\boldsymbol{\hbar\omega}$ were applied from the source (microwave generator) to the sample with a rectangular microstrip antenna, and the applied microwave power was -10 dB. The microstrip antenna was designed with different frequencies ranging from 3 GHz to 24 GHz to transmit or receive electromagnetic waves, as shown in Fig. 1.[32] The lock-in detection was used at the modulation frequency of the microwave power of 850 Hz.

Interestingly, in the high magnetic field experiments, the microwave frequencies varied between 30 and 110 GHz and were supplied by a range of backward wave oscillators. The sample was placed in a 17 T superconducting magnet and maintained at 4 K by a variable temperature insert. B_{ac} is the magnetic field component of the microwave that drives spin resonance. Rectification of the photovoltage follows from the relationship between the spatially varying ac magnetic modulation applied to the 2DEG and the eddy currents due to dB_m/dt. B_m is the fringe field at the site of the 2DEC induced by the oscillations of the magnetization, and the rectified Hall voltage was generated across the bar magnet

$$V_x = \mu\, \mu_0^2\, A\, \langle M_z \dot{M}_x - M_x \dot{M}_z \rangle\,, \qquad (1)$$

where μ_0 is the magnetic permeability, μ is the electron mobility in 2DEG, A is the active area which is approximately the square of the decay length of the stray magnetic field, and M_x and M_z are the magnetization components, as shown in Fig. 3. When B_{ac} was applied, the magnetic moment of Co precesses at a frequency ω_0 which is proportional to the magnitude of the static magnetic field plus the demagnetizing field. Then, the moment flips down and oscillates back and forth parallel and antiparallel to B_a to create peaks according to Equation 1.

2.3 Micromagnetic Simulation

Ferromagnetic resonance was simulated using OOMMF micromagnetic simulation. The OOMMF simulation solved the Landau-Lifshitz-Gilbert (LLG) nonlinear time-dependent partial differential equations of the magnetization. Spectral dependencies and spatial distribution of magnetization precession were obtained by the precession amplitude of the magnetization in the magnetic susceptibility. Magnetization could be calculated in space and time to map the evolution of

magnetization in nanosized ferromagnets. One of the advantages of finite difference simulations is the ability to measure the dephasing φ of the magnetization relative to the ac magnetic field. Thus, by using the phase difference φ to calculate the real and imaginary parts of the magnetic susceptibility

$$\chi = \frac{M}{H} = \frac{M_0}{H_0} cos\varphi + \frac{M_0}{H_0} sin\varphi \frac{cos\omega t}{sin\omega t} \ , \qquad (2)$$

$$\chi = \chi' + i\chi'' \ , \qquad (3)$$

where M(t) is the periodic magnetic response, H(t) is the periodic magnetic field, and $\boldsymbol{\omega}$ is the microwave angular frequency. Equation 3 determines the real component or in-phase χ' that gives a speed of propagation of the electromagnetic wave in the magnet, and the imaginary component χ'', or an out-of-phase that corresponds to the absorption of microwave energy. These values have been compared with the experimental absorptions. As a result, the power absorbed per the unit volume P demonstrated the relationship with imaginary susceptibility

$$P = \frac{1}{2} \omega \chi'' H_0^2 \ , \qquad (4)$$

We have simulated sample thicknesses ranging from 30nm to 220nm. At the high magnetic fields where magnetic resonance takes place (> 0.5T), the magnetization is saturated in the bulk of the sample and parallel to the plane of the interface. We find that, due to the absence of magnetic poles in the surface parallel to the GaAs/Co interface the simulated magnetic spectra are largely independent of thickness for thicknesses between 30nm and 220nm. Figure 4(a) illustrates the magnetic response of a single Co stripe with length 2040 nm, width 220 nm, and a thickness 30 nm meshed by $5 \times 5 \times 30$ nm cells for the purpose of finite element simulation. That was recorded under the action of the alternating field B_{ac} and constant field B_a in 1 ps time steps. The value of saturation magnetization of Co is $\mu_0 M_s$=1.77 T, the exchange interaction constant A = 30×10^{-12} J/m; K_1 = 0 J/m^3 (polycrystalline Co), and α is the Gilbert damping constant α = 0.05.[33, 34] The magnetization of the stripe was excited by the alternating magnetic field B_{ac} in presents of constant field B_a. A constant magnetic field was applied along the short side of the strip. The magnetic field B_a was varied in the range [-3; +3] T in steps of 0.025 T. The relaxation of the system was during

0.2 ns after each change over 20 periods of the alternating field $B_{ac} = B_0 \sin(\omega t)$.[34] Figure 4(a) also shows the magnetic simulation that was obtained at three frequencies: 41 GHz, 52 GHz, and 63 GHz in the magnetic stripe in the case alternating field of amplitude $B_{ac} = 1 \times 10^{-5}$ T. We repeated the magnetic simulation with Co disk with length 80 nm, width 80 nm, and thickness 30 nm was meshed by $2 \times 2 \times 40$ nm cells. The simulation was obtained for two frequencies, 35 GHz, and 55 GHz [Fig. 5(a)]. The dynamical characteristics of the nanostructure can be defined using fast Fourier transformation (FFT) to obtain the imaginary susceptibility $\boldsymbol{\chi''}$ as a function of the magnetic field, as shown in Equation 2. Then the phase shift of the magnetization and the microwave field were described.

3. Results and Discussion

3.1 Individual Stripe

In this section, we demonstrate an experimental SWR of the magnetic stripe at different frequencies at 4 K [Fig. 4(a)]. The creation of confined spin waves involves both the quantum mechanical exchange interaction and classical confinement by the magnetostatic potential. The exchange interaction aligns spin chains of itinerant electrons. The magnetostatic potential creates the boundary conditions confining the spin waves. The discrete energy levels produced in the confinement of spin waves are similar to those of electrons that are confined in a magnetic well. The dispersion law for dipolar-exchange spin waves, has a wavevector $\boldsymbol{q}$ parallel to the magnetic field in a thin film[22, 35]

$$\left(\frac{\omega}{\omega_M}\right)^2 = \left(\frac{\omega_H}{\omega_M} + \alpha q^2\right)\left[\frac{\omega_H}{\omega_M} + \alpha q^2 + 1 - \frac{1 - exp(-qh)}{qh}\right], \quad (5)$$

where $\omega_M = \gamma 4\pi M_s$, $\propto = 2\pi A/\mu_0 M_s^2$ is the exchange constant expressed as a function of the effective area *A*, and $\omega_H = \gamma H$. Here, *H* is the internal field including B_a and the demagnetizing field, and *M (z)* is the stray magnetic field. In addition, $\boldsymbol{q}$ has two quantized components $\boldsymbol{q_y}$, and $\boldsymbol{q_z}$, and free component $\boldsymbol{q_x}$. When ω_H is smaller than $\boldsymbol{\omega}$, $\boldsymbol{q}$ is real at the center of the stripe, but if the solution is imaginary, the spin wave is evanescent. When the internal magnetic field is the lowest, the dipolar surface spin wave propagates near the poles. The quantization of the spin wave frequency $\boldsymbol{\omega}$ gives a series of small peaks associated with localized edge spin waves. In this case, we studied the effect of applying B_a parallel to the short axis of bar magnets. The spin waves were

confined to the opposite edges and overlapped to create a bonding state localized at the center of the stripe and an antibonding state localized at the two magnetic wells on the edges, and that is indicated by labels I and II, respectively [Fig. 4].[36, 37] The bonding state is the main peak that occurs at low magnetic field whilst the antibonding state is the minor peak. Figure 4(a) shows the bonding and antbonding resonances I and II in the micromagnetic simulation at B_1 = 1.11 T and B_2 = 1.65 T (41 GHz), B_1 = 1.447 T and B_2 = 2 T (52 GHz), and B_1 = 1.87 T and B_2 = 2.4 T (63 GHz). Figure 4(b) shows the corresponding peak positions observed in the experimental photovoltage at B_1 = 1.5 T and B_2 = 1.67 T at 41 GHz, B_1 = 2 T and B_2 = 2.22 T at 52 GHz, and B_1 = 2.33 T and B_2 = 2.45 T at 63 GHz. The shift to higher magnetic field in the experimental traces is due to the magnetic anisotropy of Co. Figure 4(b) therefore displays a series of small resonances (1-5) which are associated with quantized dipolar edge spin wave modes including bonding and antibonding. The magnetic field of the resonance at different frequencies can be verified by the main peak (bonding) using the resonance equation: $B_a = \hbar\omega/(g\mu_B)$, where $\boldsymbol{\mu_B}$ is the Bohr magneton and $\boldsymbol{g}$ is the $\boldsymbol{g}$-factor. At 41 GHz the position of the calculated main peak is 1.36 T, at 52 GHz it is 1.73 T and at 63 GHz it is 2.1 T. These results show agreement between the experiment and theory considering that the experimental resonances are shifted to higher magnetic field by the magnetocrystalline anisotropy of Co. The anisotropy field may be expressed by $H_c = 2K_u/M_S\mu_0$. When K_u = 5.5 $\times$ 10^5 J.m^{-3}, at low temperature the resonance shift is H_c = 0.4T as observed. The amplitude of the resonant peaks in both micromagnetic simulations and photovoltage spectroscopy decrease with increasing frequency. Figure 4(c) presents the location of the discrete spin wave modes in 2D maps of the imaginary susceptibility at 52 GHz.[38, 39] However, the position of resonances I and II in Fig. 4(a) match the peak positions in Fig. 4(b).

In the case where B_a is parallel to the long edge of the bar magnets, the magnetostatic boundary conditions constrain spin wave modes to the surface of the magnets. The photovoltage resonances are indicated by Damon-Eshbach modes that propagate along the edges of the stripe parallel to B_a. Several distinct peaks are labelled I , II, and III, at 41GHz [Fig. 5]. Figure 5(a) indicates that the position of the resonances from OOMMF simulation are B_1 = 0.3 T, B_2 = 0.95 T, and B_3 = 1.489 T at 41 GHz, while the location of the photovoltage spectroscopy peaks [Fig. 5(b)] are B_1 = 0.85 T, B_2 = 1.5 T, and B_3 = 1.66 T at 41 GHz. Figures 4 and 5 show that when B_a is parallel to the long edge of bar magnets. The peak amplitudes are much smaller than when B_a is parallel to the

short edge. This relationship shows the spatial susceptibility distribution because of the small value and strong edge localization [Fig. 5(c)].

3.2 Micromagnetic Disk

We now consider the properties of the magnetic disk at different frequencies, at 4 K. The modulation magnetic field was generated by an 80 nm diameter Co dot. The parallel orientation is no different than the perpendicular for symmetry reasons, and this dot was magnetized in-plane, parallel to the 2DEG. In this case, a 2D potential is created at the opposite ends of the magnetized disk. A bonding state is located at the center of the disk, and the antibonding state at the site of the two magnetic wells on the edges. The locations are similar to the case when the stripes are magnetized along their short axis. These results therefore demonstrate the micromagnetic simulation as a function of the frequency. We labelled peaks in Fig. 6(a) as B_1 = 1.7 T, and B_2 = 1.95 T at 55 GHz in the theoretical plot. Experimentally, the positions of the ferromagnetic resonance peaks from photovoltage spectroscopy are B_1 = 1.64 T, and B_2 = 1.99 T at 55 GHz, in the theoretical plot. Experimentally, the position of the peak of ferromagnetic resonance in photovoltage spectroscopy are B_1 = 1.64 T, and B_2 = 1.98 T at 55 GHz, as shown in Fig. 6(b), and they are the bonding and antibonding states respectively. Figure 6(c) shows the 2D map of the magnetization oscillation amplitude for the main and minor peaks. Figures 4 and 6 demonstrate good qualitative agreement between theory and experiment in the predicted resonance positions, indicating the formation of bonding-antibonding pairs of edge spin waves. However, the amplitudes of the peaks decreased with increasing frequency. The amplitude of the photovoltage decreases as the microwave frequency increases because, at constant microwave power, P, the increase in photon energy, $\hbar\omega$, implies that fewer photons, n, are absorbed in resonance, according to the equation: $n = P / \hbar\omega$.

3.3 The Effect of Magnetocrystalline anisotropy on the ferromagnetic resonance

The magnetic anisotropy of ferromagnetic materials plays a dominant role in magnetization curves, and ferromagnetic resonance spectra. The cobalt lattice structure implies that; the easy axis is perpendicular to the plane. The anisotropiy is determined by the field required to tilt the magnetization from the easy axis to the hard axis. The effect of magnetocrystalline anisotropy on ferromagnetic resonance is more complex as precession makes the magnetization vector probe a 3D volume prior to setting in the new steady state. Anisotropy is also determined by the shape.[40)]

The long dimension of the crystal produces a lies the easy axis. In individual stripes, the easy axis is along the longest edge, which is 80 nm. The anisotropy field may be expressed by $\Delta H = 2K_u/M_s\mu_0$, where K_u is the constant anisotropy of Co; at low temperature, 5.5×10^5 Jm^3. In the case of the disk the easy axis is in the plane along the diameter, which is 80.99 nm. However, the calculation was taken by the OOMMF program at 35 GHz, with the magnetocrystalline anisotropy field perpendicular to the stripe, shifting the resonance. As shown in Fig. 7, when no anisotropy is applied, there is a single peak at the easy axis. However, by applying magnetocrystalline anisotropy in different orientations ($\langle 590\rangle, \langle 390\rangle, \langle 290\rangle, \langle 010\rangle$) different peaks appear because the resonances are shifted as the easy axis inducing shape and magnetocrystalline anisotropy tilts relative to the stripe long axis.

4. Conclusion

Our investigation has shown that photovoltage spectroscopy senses the magnetization dynamics of nanomagnets with a size of 80 nm using micron size Hall junctions. The results show that the discrete structure of spin wave resonances depends on the shape of the magnets, the magnetic field orientation to the magnetization, and the geometry of nanomagnets. The relative peak amplitudes when the magnetization is parallel to the long axis of the stripe indicate that Damon-Eshbach modes are much weaker than dipolar edge spin wave modes when B_a is parallel to the short axis. Bonding-antibonding pairs of edge spin waves are observed to form. The larger magnitude of the signal makes the field orientation parallel to the short edge easier to interpret than other orientations. Furthermore, the effect of magnetocrystalline anisotropy has shifts the resonance to a new position.

Acknowledgments

This work also was supported by FP7-2012-IRSES (U.K) under grant number 318973. Najla Almulhem acknowledges support from the Ministry of Education in Saudi Arabia, and Saudi Arabian Cultural Bureau in London for making it possible to undertake this work. This work

funded by DeanShip of scientific research (DSR), King Faisal University, Al-Hassa, KSA under grant No. 186246. Najla Almulhem thank DSR technical and financial support.

References

1) J. A. Sidles, J. L. Garbini, K. Bruland, D. Rugar, O. Züger, S. Hoen, and C. Yannoni, Rev. Mod. Phys. **67**, 249 (1995).
2) W. Zeper, F. Greidanus, P. Carcia, and C. Fincher, J. Appl. Phys. **65**, 4971 (1989).
3) P. Thibault, M. Dierolf, A. Menzel, O. Bunk, C. David, and F. Pfeiffer, Science. **321**, 379 (20018).
4) C. W. Sandweg, M. B. Jungfleisch, V. I. Vasyuchka, A. A. Serga, P. Clausen, H. Schultheiss, B. Hillebrands, A. Kreisel, and P. Kopietz, Rev. Sci. Instrum. **81**, 073902 (2010).
5) J. Kieffer, Modern Glass Characterization, 1 (2015)
6) C. Chappert, K. Le Dang, P. Beauvillain, H. Hurdequint, and D. Renard, Phys. Rev. B. **34**, 3192 (1986).
7) M. Harder, Z. X. Cao, Y. S. Gui, X. L. Fan, and C. M. Hu, Physical Review B, **84** (2011).
8) M. Harder, Y. Gui and C.-M. Hu, Physics Reports, **661**, 1 (2016).
9) Y. Tserkovnyak, A. Brataas, G.E. Bauer, and B.I. Halperin, Rev. Mod. Phys.**77**, 1375 (2005).
10) A. Chumak, V. Vasyuchka, A. Serga, and B. Hillebrands, Nat. Phys. **11**, 453 (2015).
11) P. Wessels, A. Vogel, J.-N. Tödt, M. Wieland, G. Meier, and M. Drescher, Sci Rep. **6**, 22117 (2016).
12) Y. Gui, L. Bai and C. Hu, Sci. China Phys. Mech. Astron **56**, 124 (2012).
13) Y. S. Gui, N. Mecking, X. Zhou, G. William, and C. M. Hu, Phys. Rev. Lett. **98** (2007).
14) J. Jorzick, S. O. Demokritov, B. Hillebrands, M. Bailleul, C. Fermon, K. Y. Guslienko, A. N. Slavin, D. V. Berkov, and N. L. Gorn, Phys Rev Lett. **88**, 047204 (2002).
15) X. Zhu, M. Harder, J. Tayler, A. Wirthmann, B. Zhang, W. Lu, Y. Gui, and C.-M. Hu, Phys. Rev. B. **83**, 140402 (2011).
16) D. N. Lawton, A. Nogaret, S. J. Bending, D. K. Maude, J. C. Portal, and M. Henini, Phys. Rev. B. **64**, 033312 (2001).
17) A. Nogaret, J. Phy.s Condens. Matter. **22**, 253201 (2010).
18) A. Nogaret, D. N. Lawton, D. K. Maude, J. C. Portal, and M. Henini, Phys. Rev. B. **67**, 165317 (2003).
19) D. Uzur, A. Nogaret, H. E. Beere, D. A. Ritchie, C. H. Marrows, and B. J. Hickey, Phys. Rev. B. **69** (2004).
20) R. W. Damon, and J. Eshbach, J. Phys. Chem. Solids, **19**, 308 (1961).

21) J. Eshbach, and R. Damon, Phys. Rev. **118**, 1208 (1960).
22) C. Bayer, J. Jorzick, S.O. Demokritov, A.N. Slavin, K.Y. Guslienko, D.V. Berkov, N.L. Gorn, M.P. Kostylev, and B. Hillebrands, *Spin dynamics in confined magnetic structures III* (Springer, Heidelberg, 2006), p. 57.
23) M. J. Donahue, OOMMF user's guide, version 1.0, 1999.
24) J. Henning, and J. Den Boef, J. App. phys. **16**, 353 (1978).
25) C. Chappert, and P. Bruno, J. Appl. Phys. **64**, 5736 (1988).
26) R. S. de Biasi, and T. C. Devezas, J. Appl. Phys. **49** (1978).
27) P. Saraiva, A. Nogaret, J. C. Portal, H. E. Beere, and D. A. Ritchie, Phys. Rev. B. **82**, 224417 (2010).
28) J. P. Park, P. Eames, D. M. Engebretson, J. Berezovsky, and P. A. Crowell, Phys. Rev. lett. **89**, 277201 (2002).
29) A. Awad, G. Aranda, D. Dieleman, K. Guslienko, G. Kakazei, B. Ivanov, and F. Aliev, App. Phys. Lett. **97**, 132501 (2010).
30) A. A. Awad, A. Lara, V. Metlushko, K. Y. Guslienko, and F. G. Aliev, App. Phys. Lett. **100**, 262406 (2012).
31) D. Backes, R. Hall, M. Pepper, H. Beere, D. Ritchie, and V. Narayan, J. Phys. Condens. Matter. **28**, 01LT01 (2016).
32) I. Singh, and V. S. Tripathi, *Int. J. Comput. Technol.* Adv. Eng. Appl, **2**, 1595 (2011).
33) S. Michea, J. Briones, J. Palma, R. Lavín, J. Escrig, R. Rodríguez-Suárez, and J. C. Denardin, arXiv preprint arXiv:1401.6064 (2014).
34) M. E. Stebliy, S. Jain, A. G. Kolesnikov, A. V. Ognev, A. S. Samardak, A. V. Davydenko, E. V. Sukovatitcina, L. A. Chebotkevich, J. Ding, J. Pearson, V. Khovaylo, and V. Novosad, Sci Rep. **7**, 1127 (2017).
35) B. Kalinikos, and A. Slavin, J. Phys. C: Solid State Phys. **19**, 7013 (1986).
36) J. A. C. Bland, A. Hirohata, Y. B. Xu, C. M. Guertler, and S. N. Holmes, IEEE trans. magn. **36**, 2827 (2000).
37) A. Nogaret, M. Stebliy, J. C. Portal, A. Samardak, A. Ognev, H. Beere, and D. Ritchie, Solid State Phenomena. **215**, 400 (2014).
38) A. Kaya, and J. A. Bain, J. App. Phys. **99**, 08B708 (2006),
39) B. Zhang, W. Wang, C. Mu, Q. Liu, and J. Wang, J. Magn. Magn. Mater. **322**, 2480 (2010).

40) N. A. Spaldin, Magnetic materials: fundamentals and applications, Cambridge University Press (2010).

Figure Captions

Fig. 1. The rig setup consists of two permanent magnets NdFeB, with the sample placed midway between the two NdFeB magnets. Above the sample is a microwave antenna holder. The Whitworth screw displaces magnets horizontally. The cold finger is used for cooling the sample to liquid nitrogen temperature. The inset shows one rectangular microstrip antenna we designed with frequency of 12 GHz.

Fig. 2. a) The SEM image of a Hall bar device used for photovoltage spectroscopy measurements. V_x is taken at the probe separation of 8 μm. The black square indicates the location of Co (stripe or dot). (b) High resolution SEM of Co stripe across the Hall channel region between the voltage probes. The stripe is 80 nm wide and 30 nm thick. (c) The Co dot that has a diameter of 80.99 nm, and a thickness of 40 nm.

Fig. 3. Schematic of the magnetic dot (Co) magnetized in the plane of the 2DEG by B_a and driven to resonance by B_{ac}. Magnetic moments *M* undergo precession at frequency ω_0 in magnetic field B_a.

Fig. 4. a) Simulation of imaginary susceptibility as a function of the magnetic field B_a (parallel to the short edge) for different frequencies in the bar magnet. b) Photovoltage spectroscopy of magnetic excitation in a parallel magnetic field B_a. c) Spatial distribution of magnetization oscillation amplitude for 52 GHz.

Fig. 5. a) Simulation of imaginary susceptibility as a function of magnetic field (B_a parallel to the long edge). b) Photovoltage spectroscopy of magnetic excitation in A parallel magnetic field B_a. c) Spatial distribution of magnetization oscillation amplitude all taken at 41 GHz.

Fig. 6. a) Simulation of imaginary susceptibility as a function of magnetizing field B_a. The dot was magnetized in-plane parallel to the 2DEG for different frequencies. b) Photovoltage spectroscopy of magnetic excitation was magnetized in-plane parallel to the 2DEG. c) Spatial distribution of magnetization oscillation amplitude for 55 GHz.

Fig. 7. Ferromagnetic spectroscopy calculated at 35 GHz under the magnetocrystalline anisotropy field that shifts the resonance peak to the new position.

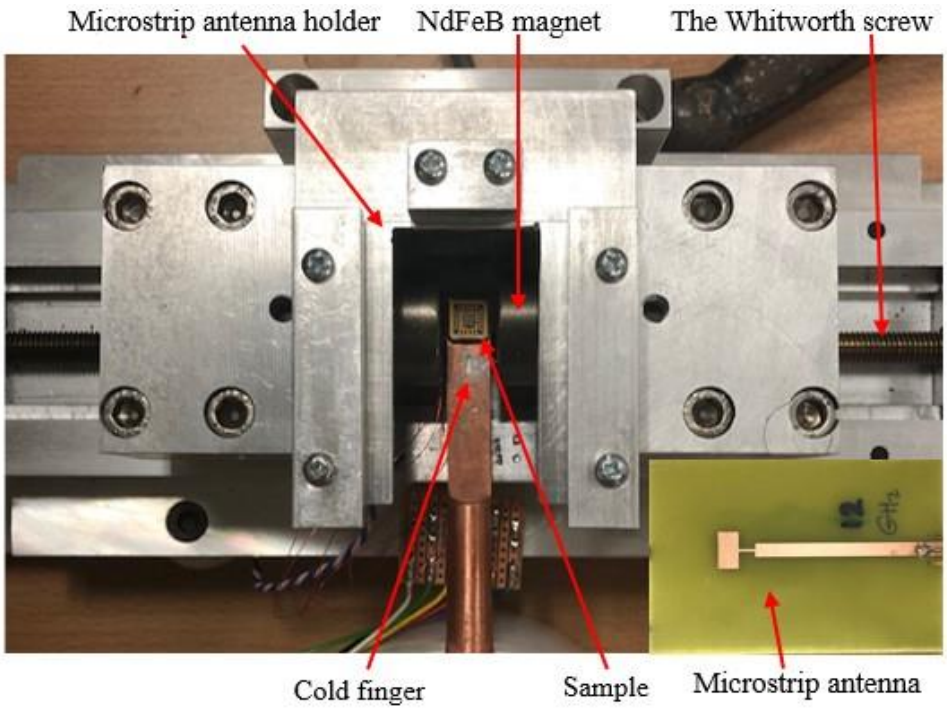

Fig.1. (Color Online)

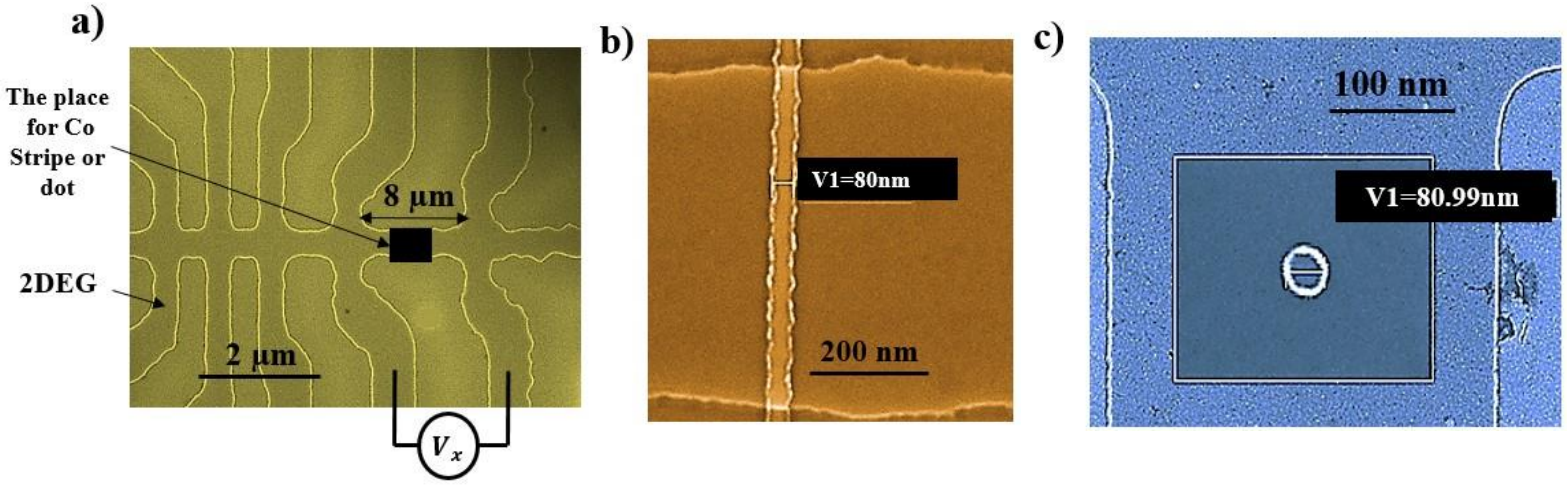

Fig.2. (Color Online)

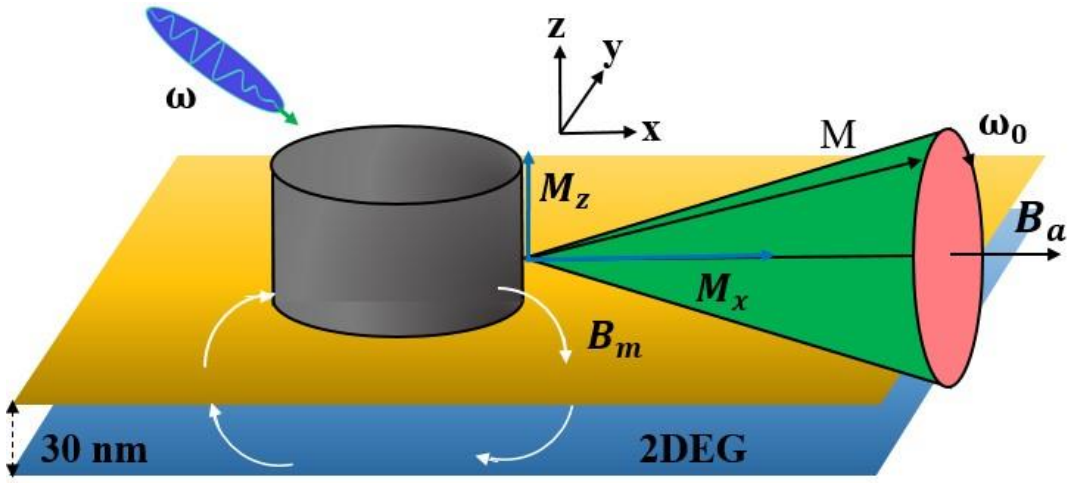

Fig.3. (Color Online)

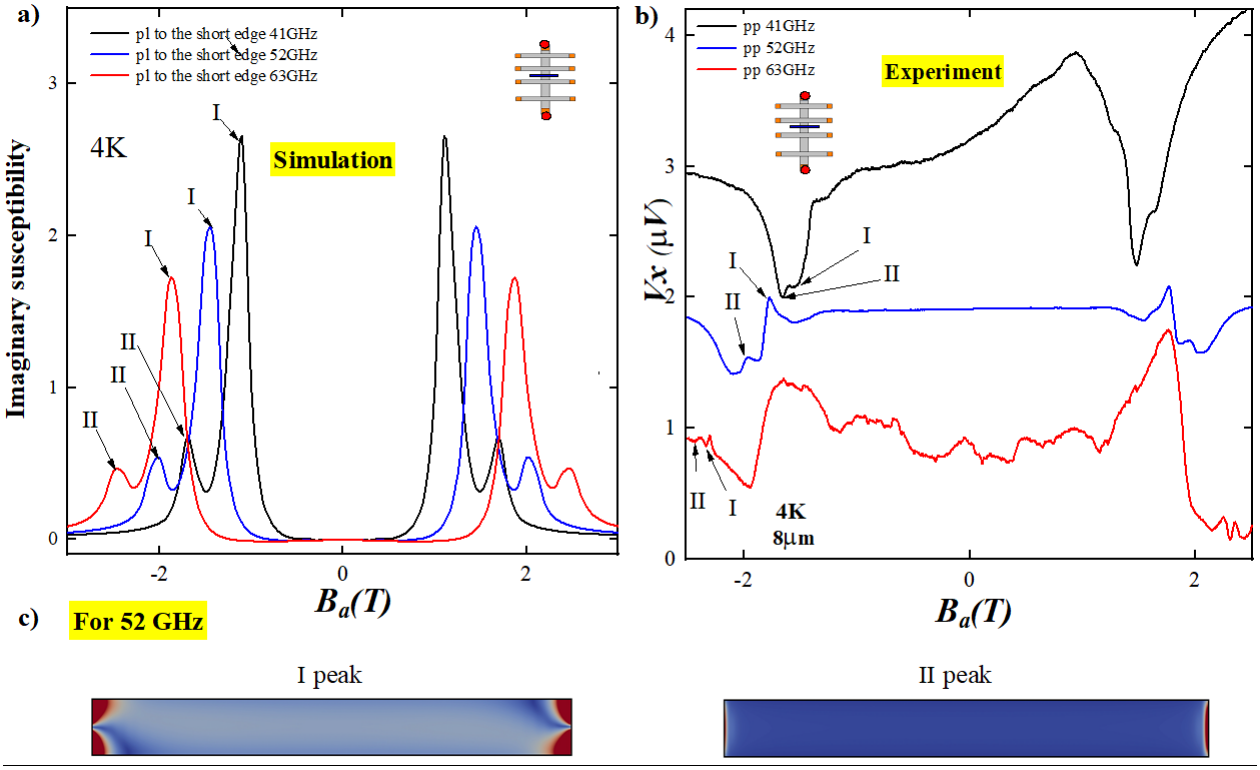

Fig.4. (Color Online)

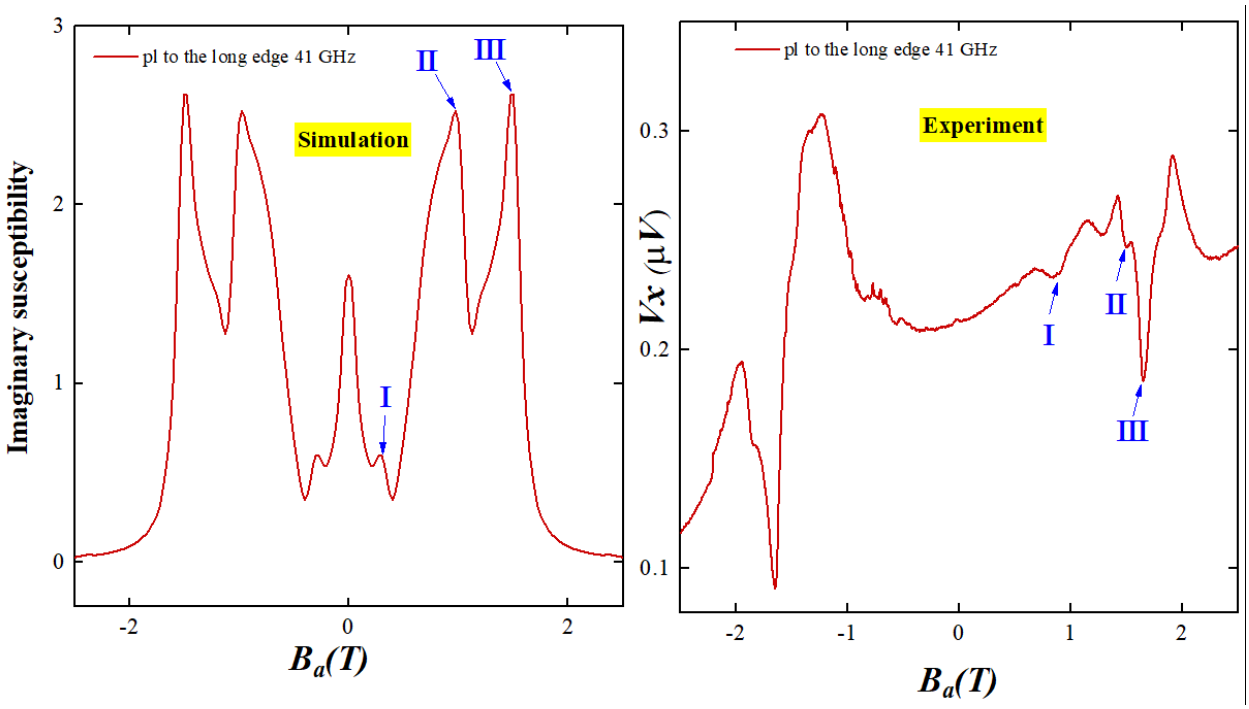

Fig.5. (Color Online)

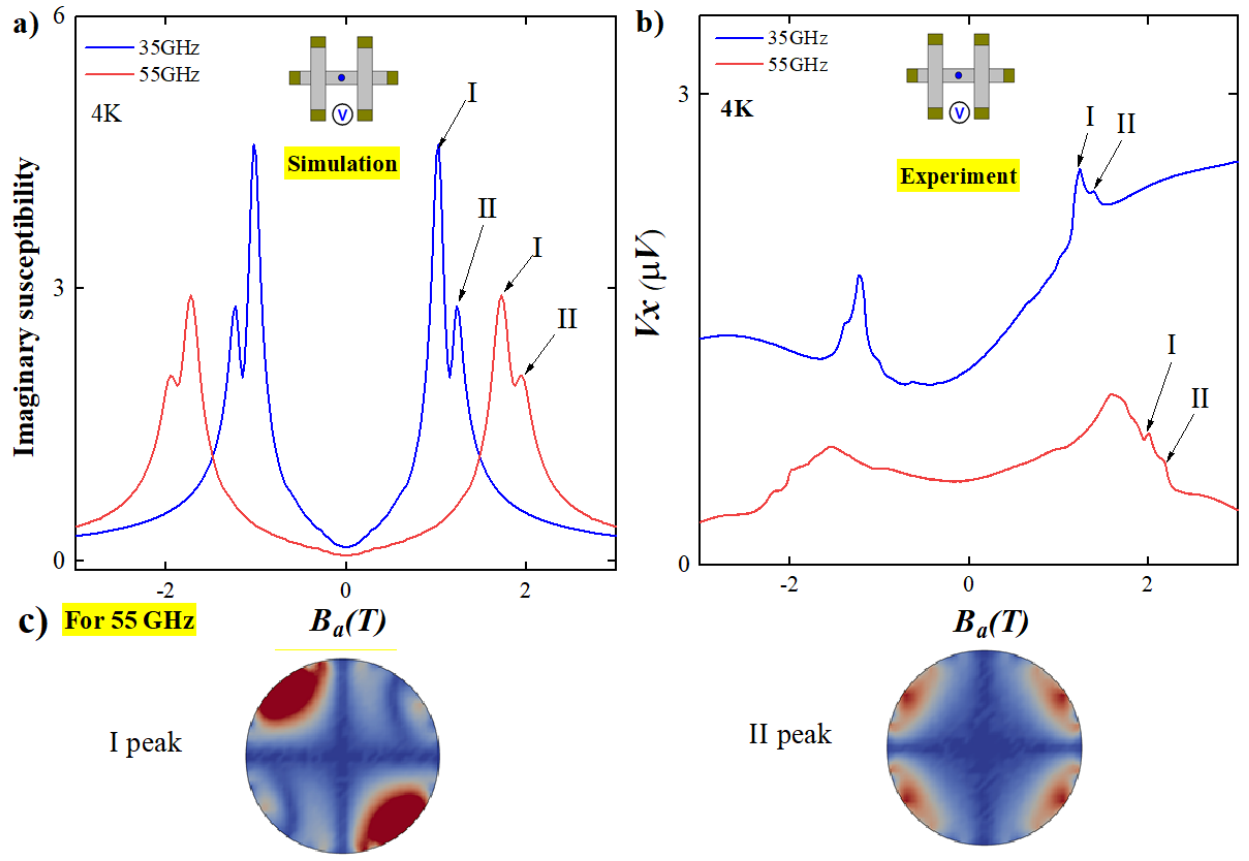

Fig.6. (Color Online)

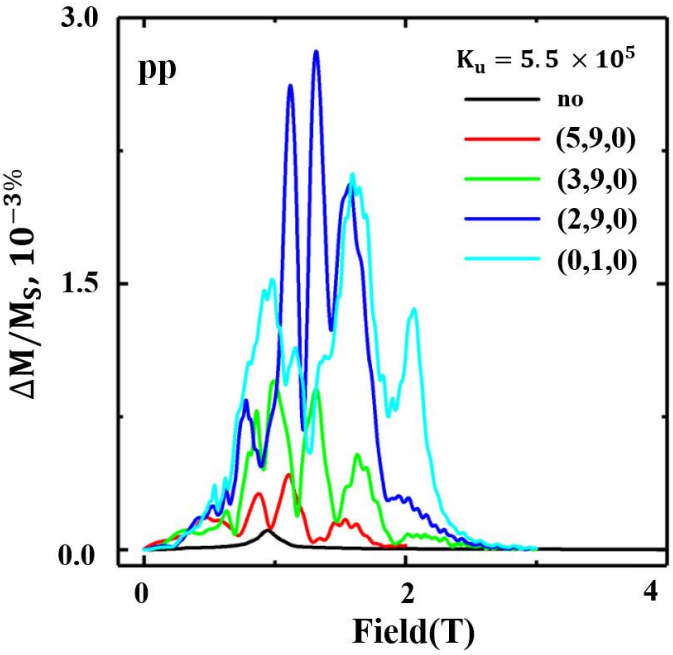

Fig.7. (Color Online)